

**Time reversal imaging in stratified waveguide under the mismatches of sound  
speed profile and array shape**

Yingzi Ying<sup>a)</sup>

*Mathematical and Computer Sciences and Engineering Division,*

*King Abdullah University of Science and Technology,*

*Thuwal,*

*Jeddah 23955,*

*Saudi Arabia*

(Dated: April 8, 2012)

## **Abstract**

The random perturbations of sound speed profile and array shape could disturb received signal, which prevent us from accurately imaging or locating long distance active sources in shallow water waveguides. In this paper, the coherent summation of virtual time reversal fields over the frequency band of probe signal is introduced as an imaging estimator to overcome difficulties caused by model inaccuracies. A mode perturbation theory is adopted to analyze the effects of sound speed profile mismatch on retrofocusing field, and the influence of array shape mismatch is also taken into consideration. The results of numerical simulations under different circumstances show the images would highlight the focal spots and the background is also smoothed, which enable us to locate source positions accurately. To improve the image quality deteriorated by sound speed profile mismatch, the perturbed modes are filtered out, and the processing results show the focal spots become more bright and the side lobes are suppressed.

PACS numbers: 43.30.Bp, 43.60.Gk, 43.60.Jn

Keywords: Virtual time reversal, Source imaging, Perturbation theory, Mode filtering

## Introduction

Remote source imaging in shallow water waveguide has become one of the most important issues and been extensively studied in the underwater acoustics communities. The imaging process is an inverse problem that we reconstruct the unknown source distribution and intensity by utilizing signal received by an array. The imaging methods could be classified into two general categories in underwater water acoustics: coherent imaging methods and incoherent imaging methods. The coherent imaging could be performed in the time domain which use time delay and amplitude information of broadband signal, such as wideband synthetic aperture sonar<sup>1</sup>, or with the fixed frequency method based on the phase differentiation at different array elements, such as beamforming<sup>2</sup>. The incoherent imaging methods only make use of the signal intensity information.

One of the most popular source imaging methods in underwater waveguide is done through matched field processing<sup>3,4</sup>, in which the acoustic pressure signal received by an array is matched with the replicas generated by some acoustic models to estimate unknown parameters of source positions in the searching space. This method utilizes the physics of wave propagation that the complexity of the ocean environment can be exploited to improve the imaging performance compared with the traditional methods based on plane wave hypothesis. But matched field processing needs prior environmental information and is sensitive to the inaccuracies of model parameters, such as sound speed, array shape, and bathymetry, etc., and the imaging result could be deteriorated dramatically even under small mismatches. For example, the mismatch in bathymetry can lead mirage in the estimated position<sup>5</sup>.

Temporal and spatial retrofocusing properties of acoustic time reversal has long been a prevailing concept and become fruitful in underwater acoustics<sup>6-9</sup>. In physical time reversal, which is also referred as phase conjugation in the frequency domain, we use an array to receive the signal which is emanated by a sound source in ocean waveguide, then reverse the

---

<sup>a)</sup>Electronic address: yingzi.ying@kaust.edu.sa

recorded signal in the time domain and transmit it back into the real medium. If the ocean environment is static, and the array shape remains unchanged in receiving and emanating procedures, the retransmitted wave will converge back to the original source position. This is due to the time reversal invariance of linear acoustic wave equation and the reciprocity principle of acoustic field<sup>10</sup>. The physical time reversal process is self-adaptive, which does not need to acquire prior knowledge of the complex waveguide environment, as the ocean itself will construct the replica field<sup>11</sup>. The retrofocusing field in static inhomogeneous waveguide will exhibit super-resolution phenomena<sup>12</sup>, and is also statistical stable or self-average in broadband regimes, that the retrofocusing field is independent of the particular realizations of inhomogeneous waveguide<sup>13,14</sup>.

The spatial retrofocusing characteristic of acoustic time reversal gives us a hint to image active sources at unknown locations. We receive the signal through an array and sent back a time reversed version into a fictitious waveguide with a fictitious array. This is the so-called virtual time reversal that the back-propagation is done numerically in a reference medium. If the models of fictitious waveguide and array shape are exactly the same as the actual ones, the waves will trace back and peak at the source positions in fictitious waveguide, thus the focal spots would point out original source positions.

Nevertheless, this imaging strategy need exact environmental information and actual array shape, which might be unavailable or errors exist in practical situations. For instance, the internal surface waves and measurement errors in conductivity-temperature-depth (CTD) casts could cause sound speed profile perturbation. Usually, sufficient and accuracy bottom geo-acoustic parameters are not easy to obtain, which will increase the inaccuracy of waveguide model. Sometimes, we only have historical data set on hand rather than up-to-date environmental information of experiment area. The dynamic ocean effects will cause the array drifts away from equilibrium position, thus introduce spatial sampling perturbation. The mismatches between the adopted models and the real situations will deteriorate retrofocusing result, that the virtual time reversal field becomes impracticable to image underwater sources.

In order to overcome the difficulties caused by model mismatches, we try to sum up or take the average value of the retrofocusing fields to highlight focal spots and smooth heterogeneous background. The coherent summation of virtual time reversal fields over the frequency band of probe signal is adopted as the imaging estimator. We will see that it is a reduced form of coherent interferometry, which migrates the crosscorrelations of the traces over some space-time windows and has been proved to work well in scattering media<sup>15–18</sup>

This paper is organized as follows: In Sec. I, the influences of sound speed profile and array shape mismatches on virtual time reversal field are analyzed. Sec. II presents the imaging algorithm and numerical simulations under four circumstances. In Sec. III, we provide a mode filtering method to improve image quality deteriorated by sound speed mismatch. Last section summarizes our conclusions.

## I. VIRTUAL TIME REVERSAL FIELD UNDER SOUND SPEED AND ARRAY SHAPE MISMATCHES

We mainly consider two main perturbations in shallow water waveguide: sound speed profile mismatch and array shape mismatch. This section is intended to analyze their influences on virtual time reversal fields. The sound speed profile mismatch will cause the Green's function perturbation between the sources and the receivers, and the array shape mismatch will cause spatial sampling perturbation. Assume the probe signal  $f_i(\omega)$  is emanated by the  $i$ th source at  $\mathbf{r}_{si}$ , the sound pressure signal received by array is

$$p(\mathbf{r}_0 + \Delta\mathbf{r}) = \sum_i f_i(\omega)(g_0(\mathbf{r}_0 + \Delta\mathbf{r}, \mathbf{r}_{si}; \omega) + \Delta g(\mathbf{r}_0 + \Delta\mathbf{r}, \mathbf{r}_{si}; \omega)), \quad (1)$$

where  $\Delta\mathbf{r}$  is the array shape perturbation off the equilibrium position  $\mathbf{r}_0$ , and  $\Delta g$  is the Green's function perturbation between the actual waveguide and fictitious model  $g_0$ . Here the subscript 0 denotes the unperturbed model.

The back-propagation is performed numerically in a fictitious waveguide through a fictitious array, which emanates the time reversed signal at the equilibrium position. The virtual

time reversal field at the searching position  $\mathbf{r}$  is

$$\Gamma(\mathbf{r}, \omega) = \int_{\mathcal{A}_0} d\mathbf{r}_0 \sum_i f_i^*(\omega) (g_0^*(\mathbf{r}_0 + \Delta\mathbf{r}, \mathbf{r}_{si}; \omega) + \Delta g^*(\mathbf{r}_0 + \Delta\mathbf{r}, \mathbf{r}_{si}; \omega)) g_0(\mathbf{r}, \mathbf{r}_0; \omega), \quad (2)$$

and  $\mathcal{A}_0$  denotes the fictitious array at the equilibrium position. Eq. (2) can also be described as the point spread function<sup>19</sup>.

In case of static waveguide and array shape, the unperturbed virtual time reversal field becomes

$$\Gamma_0(\mathbf{r}, \omega) = \int_{\mathcal{A}_0} d\mathbf{r}_0 \sum_i f_i^*(\omega) g_0^*(\mathbf{r}_0, \mathbf{r}_{si}; \omega) g_0(\mathbf{r}, \mathbf{r}_0; \omega). \quad (3)$$

In the following parts, we will analyze the effects of the mismatches of sound speed profile and array shape on virtual time reversal field, respectively. Here, for simplicity, we only take single source case into consideration.

## A. Effect of sound speed profile mismatch

In this part, the effect of sound speed profile mismatch on virtual time reversal field is analyzed. We first give the relationship between the mismatch of sound speed profile and the perturbations of horizontal wavenumber and normal mode shape function, which characterize the wave propagation in ocean waveguide. The procedures adopted here are similar to those used in deriving new normal modes at each range step in range-dependent waveguide<sup>20</sup>.

Figure 1 depicts the mismatch between the sound speed profiles of the actual and fictitious waveguides. We take the Pekeris waveguide with the constant sound speed of 1500 m/s and the density of 1000 kg/m<sup>3</sup> in the water column of 100 m depth, together with pressure-released ocean surface and liquid bottom with the longitudinal wave speed of 2000 m/s, the density of 2000 kg/m<sup>3</sup> and the attenuation of 0.3 dB/λ, as the fictitious waveguide model. The selected fictitious model may not be always exactly the same as the actual physical waveguide, in which the actual sound speed in water column is fluctuating around the fictitious model.

## 1. Horizontal wavenumber and mode shape perturbations

Assume the sound speed profile of the unperturbed waveguide is  $c_0(z)$ , the unperturbed normal mode shape function  $\varphi_{0m}$  satisfies the depth-separated wave equation<sup>21,22</sup>

$$\rho(z) \frac{d}{dz} \left( \frac{1}{\rho(z)} \frac{d\varphi_{0m}(z)}{dz} \right) + \left( \frac{\omega^2}{c_0^2(z)} - k_{0m}^2 \right) \varphi_{0m}(z) = 0, \quad (4)$$

where  $\rho(z)$  is the density and  $k_{0m}$  is the horizontal wavenumber.

The upper pressure-released boundary condition of the ocean waveguide is

$$\varphi_{0m}(0) = 0, \quad (5)$$

and the lower liquid half-space boundary condition requires

$$\varphi_{0m}(D^-) = \varphi_{0m}(D^+), \quad (6)$$

$$\rho^{-1}(D^-) [d\varphi_{0m}(z)/dz]_{z=D^-} = \rho^{-1}(D^+) [d\varphi_{0m}(z)/dz]_{z=D^+}, \quad (7)$$

where  $D$  is the bottom depth.

The horizontal wavenumber  $k_{0m}$  and normal mode shape function  $\varphi_{0m}$  are in fact the eigenvalue and eigenfunction of the system, respectively, which characterize the fictitious waveguide.

Due to the environmental perturbations and measurement errors, there could be sound speed profile perturbation  $\Delta c(z)$  between the fictitious and actual waveguides, which introduces mode shape function perturbation  $\Delta\varphi_m(z)$  and horizontal wavenumber perturbation  $\Delta k_m$ . The perturbed depth-separated wave equation becomes

$$\rho(z) \frac{d}{dz} \left( \frac{1}{\rho(z)} \frac{d(\varphi_{0m}(z) + \Delta\varphi_m(z))}{dz} \right) + \left( \frac{\omega^2}{(c_0(z) + \Delta c(z))^2} - (k_{0m} + \Delta k_m)^2 \right) (\varphi_{0m}(z) + \Delta\varphi_m(z)) = 0. \quad (8)$$

Subtracting Eq. (4) from Eq. (8) gives the expression

$$\begin{aligned} \rho(z) \frac{d}{dz} \left( \frac{1}{\rho(z)} \frac{d\Delta\varphi_m(z)}{dz} \right) + \left( \frac{\omega^2}{(c_0(z) + \Delta c(z))^2} - \frac{\omega^2}{c_0^2(z)} - (\Delta k_m)^2 - 2k_{0m}\Delta k_m \right) \varphi_{0m}(z) \\ + \left( \frac{\omega^2}{(c_0(z) + \Delta c(z))^2} - k_{0m}^2 - (\Delta k_m)^2 - 2k_{0m}\Delta k_m \right) \Delta\varphi_m(z) = 0. \end{aligned} \quad (9)$$

The unperturbed normal mode shape functions form a complete set  $\{\varphi_{0m}\}$ , which could be used to expand the mode perturbation

$$\Delta\varphi_m(z) = \sum_{m'} a_{mm'} \varphi_{0m'}(z). \quad (10)$$

Combining Eq. (10) with Eq. (4) gives

$$\begin{aligned} \rho(z) \frac{d}{dz} \left( \frac{1}{\rho(z)} \frac{d\Delta\varphi_m(z)}{dz} \right) &= \sum_{m'} a_{mm'} \rho(z) \frac{d}{dz} \left( \frac{1}{\rho(z)} \frac{d\varphi_{0m'}(z)}{dz} \right) \\ &= - \sum_{m'} a_{mm'} \left( \frac{\omega^2}{c_0^2(z)} - k_{0m'}^2 \right) \varphi_{0m'}(z). \end{aligned} \quad (11)$$

By substituting Eqs. (10) - (11) into Eq. (9), we obtain

$$\begin{aligned} \sum_{m'} a_{mm'} \varphi_{0m'}(z) \left( \frac{\omega^2}{(c_0(z) + \Delta c(z))^2} - \frac{\omega^2}{c_0^2(z)} + k_{0m'}^2 - k_{0m}^2 - (\Delta k_m)^2 - 2k_{0m} \Delta k_m \right) \\ + \left( \frac{\omega^2}{(c_0(z) + \Delta c(z))^2} - \frac{\omega^2}{c_0^2(z)} - (\Delta k_m)^2 - 2k_{0m} \Delta k_m \right) \varphi_{0m}(z) = 0 \end{aligned} \quad (12)$$

Since we only assume small environmental change, the perturbation of the horizontal wavenumber is negligible compared with itself. Keeping the leading order terms, we have

$$k_{0m}^2 + 2k_{0m} \Delta k_m + (\Delta k_m)^2 \approx k_{0m}^2, \quad (13)$$

$$2k_{0m} \Delta k_m + (\Delta k_m)^2 \approx 2k_{0m} \Delta k_m, \quad (14)$$

and

$$\Delta q(z) = \frac{\omega^2}{(c_0(z) + \Delta c(z))^2} - \frac{\omega^2}{c_0^2(z)} \ll \kappa_{0m'}^2 - \kappa_{0m}^2, \quad (15)$$

for different horizontal wavenumbers. Here the horizontal wavenumber, which is complex due to the lossy ocean bottom, is divided into real and imaginary parts, i.e.,  $k_{0m} = \kappa_{0m} + i\gamma_{0m}$ .

Then Eq. (12) is simplified as

$$\sum_{m' \neq m} a_{mm'} \varphi_{0m'}(z) (k_{0m'}^2 - k_{0m}^2) + (\Delta q(z) - 2k_{0m} \Delta k_m) \varphi_{0m}(z) = 0. \quad (16)$$

The weighted inner product of the normal mode shape functions satisfy the orthonormal condition

$$(\varphi_{0m}(z), \varphi_{0m'}(z)) = \int_0^D dz \rho^{-1}(z) \varphi_{0m}(z) \varphi_{0m'}(z) = \delta_{mm'}, \quad (17)$$



where  $\delta_{mm'}$  is the Kronecker delta function. By applying the operators  $(\cdot, \varphi_{0m'}(z))$  and  $(\cdot, \varphi_{0m}(z))$  to the both side of Eq. (16), respectively, we get

$$a_{mm'} (k_{0m'}^2 - k_{0m}^2) + (\Delta q(z) \varphi_{0m}(z), \varphi_{0m'}(z)) = 0, \quad m \neq m', \quad (18)$$

$$(\Delta q(z) \varphi_{0m}(z), \varphi_{0m}(z)) - 2k_{0m} \Delta k_m = 0. \quad (19)$$

Solving above two equations arrives at

$$a_{mm'} = \frac{(\Delta q(z) \varphi_{0m}(z), \varphi_{0m'}(z))}{k_{0m}^2 - k_{0m'}^2}, \quad m \neq m', \quad (20)$$

$$\Delta k_m = \frac{(\Delta q(z) \varphi_{0m}(z), \varphi_{0m}(z))}{2k_{0m}}. \quad (21)$$

For the  $m$ th order unperturbed mode shape function  $\varphi_{0m}(z)$ , there are  $m$  zeros in the integral interval  $[0, D]$ . If we assume slow change of  $\Delta q(z)$  in depth, thus the integrations in above two equations vanish for large mode number, that the mode shape functions and horizontal wavenumbers will become convergent.

Figure 2 shows the mode shape functions of orders 1, 2, 4, 8 and 16, where the solid curves are the perturbed mode shape functions while the dashed curves are unperturbed ones. We find that due to the sound speed profile mismatch, the fictitious mode shape functions are not in accordance with actual ones. In lower orders, the respective modes discriminate with each other considerably. When the order number increases, the sameness raises, and in higher orders the two become alike.

## 2. Virtual time reversal field under sound speed profile mismatch

The Green's function between the source at  $\mathbf{r}_s = (r_s, z_s)$  and the receiver element of an unperturbed array at equilibrium position  $\mathbf{r}_0 = (r_0, z_0)$  in range-independent, azimuthally symmetric waveguide could be expressed as<sup>22</sup>

$$g(\mathbf{r}_0, \mathbf{r}_s; \omega) = \frac{i}{\rho(z_s) \sqrt{8\pi (r_0 + r_s)}} e^{-i\pi/4} \sum_m \varphi_m(z_s) \varphi_m(z_0) \frac{e^{ik_m(r_0 + r_s)}}{\sqrt{k_m}}, \quad (22)$$

in the far field.

Similarly, the unperturbed Green's function between  $\mathbf{r}_0$  and the searching point  $\mathbf{r} = (r, z)$  in the fictitious waveguide is

$$g_0(\mathbf{r}, \mathbf{r}_0; \omega) = \frac{i}{\rho(z_0) \sqrt{8\pi (r_0 + r)}} e^{-i\pi/4} \sum_{m'} \varphi_{0m'}(z) \varphi_{0m'}(z_0) \frac{e^{ik_{0m'}(r_0+r)}}{\sqrt{k_{0m'}}}. \quad (23)$$

For a point probe source emanating the signal  $f(\omega)$ , the retrofocusing field is

$$\begin{aligned} \Gamma(\mathbf{r}, \omega) &= \int_{\mathcal{A}_0} d\mathbf{r}_0 f^*(\omega) g^*(\mathbf{r}_0, \mathbf{r}_s; \omega) g_0(\mathbf{r}, \mathbf{r}_0; \omega) \\ &= \frac{f^*(\omega)}{8\pi} \int_{z_{0\min}}^{z_{0\max}} dz_0 \frac{\varphi_m(z_0) \varphi_{0m'}(z_0)}{\rho(z_0)} \sum_{m, m'} \frac{\varphi_m(z_s) \varphi_{0m'}(z) e^{ik_{0m'}(r_0+r) - ik_m^*(r_0+r_s)}}{\rho(z_s) \sqrt{(r_0 + r_s)(r_0 + r)} \sqrt{k_m^* k_{0m'}}}. \end{aligned} \quad (24)$$

Assume the array spans almost over the whole water column, and the actual and fictitious mode shape functions are quasi-orthonormal, we have

$$\int_{z_{0\min}}^{z_{0\max}} dz_0 \frac{\varphi_m(z_0) \varphi_{0m'}(z_0)}{\rho(z_0)} \approx \delta_{m'm}. \quad (25)$$

Thus Eq. (24) is reduced as

$$\Gamma(\mathbf{r}, \omega) \approx \frac{f^*(\omega)}{8\pi} \sum_m \frac{\varphi_m(z_s) \varphi_{0m}(z) e^{-\gamma_{0m}(r_0+r) - \gamma_m(r_0+r_s)} e^{i(\kappa_{0m}(r_0+r) - \kappa_m(r_0+r_s))}}{\rho(z_s) \sqrt{(r_0 + r_s)(r_0 + r)} \sqrt{k_m^* k_{0m}}}, \quad (26)$$

If we ignore changes of mode shape function and horizontal wavenumber in the amplitude term, but keep the variation in the phase term, we get

$$\Gamma(\mathbf{r}, \omega) \approx f^*(\omega) \sum_m A_{0m} e^{i(\kappa_{0m}(r_0+r) - \kappa_m(r_0+r_s))}, \quad (27)$$

where the amplitude coefficient is

$$A_{0m} = \frac{\varphi_{0m}(z_s) \varphi_{0m}(z) e^{-\gamma_{0m}(2r_0+r+r_s)}}{8\pi \rho(z_s) \sqrt{(r_0 + r_s)(r_0 + r)} |k_{0m}|}. \quad (28)$$

The intensity field of the retrofocusing field near the probe source can be expressed as

$$I(\mathbf{r}, \omega) = \Gamma(\mathbf{r}, \omega) \Gamma^*(\mathbf{r}, \omega) \approx |f(\omega)|^2 \left( \sum_m A_{0m}^2 + 2 \sum_{m \neq m'} A_{0m} A_{0m'} \cos(\Delta\kappa_{0mm'}(r_0 + r) - \Delta\kappa_{mm'}(r_0 + r_s)) \right), \quad (29)$$

where  $\Delta\kappa_{0mm'} = \kappa_{0m} - \kappa_{0m'}$  and  $\Delta\kappa_{mm'} = \kappa_m - \kappa_{m'}$  are the differences of the real parts of different fictitious and actual horizontal wavenumbers, respectively.

If there is no sound speed profile mismatch, the unperturbed virtual time reversal field is

$$\Gamma_0(\mathbf{r}, \omega) = f^*(\omega) \sum_m A_{0m} e^{i\kappa_{0m}(r-r_s)}, \quad (30)$$

and the intensity field becomes

$$I_0(\mathbf{r}, \omega) = \Gamma_0(\mathbf{r}, \omega) \Gamma_0^*(\mathbf{r}, \omega) = |f(\omega)|^2 \left( \sum_m A_{0m}^2 + 2 \sum_{m \neq m'} A_{0m} A_{0m'} \cos(\Delta\kappa_{0mm'}(r - r_s)) \right). \quad (31)$$

From Eq. (31) we can see that at the source range  $r = r_s$ , the phase term is eliminated, which means different modes arrive in phase and virtual time reversal intensity field peaks at source range in unperturbed waveguide.

Nevertheless, owing to the horizontal wavenumber perturbation, the phase difference of each mode propagating at source range can not be canceled, as indicated in Eq. (29). Thus the virtual time reversal field might not retrofocus at source range and be degraded.

For an ideal waveguide with rigid or pressure released boundary, the mode shape functions satisfy the closure property,

$$\sum_m \frac{\varphi_{0m}(z_s) \varphi_{0m}(z)}{\rho(z_s)} = \delta(z - z_s), \quad (32)$$

where  $\delta$  is the Dirac delta function. Eq. (32) indicates the focal spot is at the probe source depth. Due to the mode shape function mismatch, the focal spot might not be at source depth.

Figure 3 (b) presents a snapshot of virtual time reversal field under the mismatch of sound speed profile. We see the focal spot, which could be clearly identified in Fig. 3 (a) in unperturbed waveguide, becomes almost invisible, that we can not locate source position through the retrofocusing field in case there is sound speed profile mismatch.

## B. Effects of array sampling position mismatch

Due to the dynamic of experimental ocean environment, the actual array might drift away from the fictitious one at the equilibrium position, which will deteriorate virtual time

reversal field. Most of the time, we even don't have enough prior knowledge to estimate array shape. In this part, we analyze the effect of array shape mismatch on the retrofocusing field. The array shape perturbation  $\Delta\mathbf{r}$  causes acoustic pressure difference  $\Delta p(\omega)$

$$p(\mathbf{r}_0 + \Delta\mathbf{r}, \omega) = f(\omega)g_0(\mathbf{r}_0, \mathbf{r}_s; \omega) + \Delta p(\omega). \quad (33)$$

Here we assume small random array shape perturbation and it is position independent, then the time reversed and back-propagated field in fictitious waveguide near the probe source position could be expressed as

$$\begin{aligned} \Gamma(\mathbf{r}, \omega) &= \int_{\mathcal{A}_0} d\mathbf{r}_0 p^*(\mathbf{r}_0 + \Delta\mathbf{r}, \omega) g_0(\mathbf{r}, \mathbf{r}_0; \omega) \\ &= \Gamma_0(\mathbf{r}, \omega) + \Delta p^*(\omega) \int_{\mathcal{A}_0} d\mathbf{r}_0 g_0(\mathbf{r}, \mathbf{r}_0; \omega). \end{aligned} \quad (34)$$

We can see that in the presence of random array shape perturbation, the virtual time reversal field is equivalent to the unperturbed one added by a random field.

Figure 4 illustrates the mismatch between actual and fictitious array shapes. The acoustic pressure field generated by the active source is sample by an perturbed array, then the received signal is time reversed and sent back with a fictitious array. In our numerical simulations, the vertical array is located at 8 km range and spans from 20 to 80 m with 2 m element step. The perturbation of each element position of discrete array conforms the uniform distribution  $\Delta\mathbf{r}_i \sim \mathcal{U}([-\Delta r, \Delta r] \times [-\Delta z, \Delta z])$ , where the horizontal and vertical maximum drifts are given as  $\Delta r = 3$  m and  $\Delta z = 1$  m, respectively.

Figure 3 (c) shows a virtual time reversal field snapshot under the array shape mismatch, in which a lot of spurious spots appear. The faintness of retrofocusing spot prevents us to identify the original source position.

The degradation of virtual time reversal field is depend on the particular realizations of the mismatches of sound speed profile and array shape. For example, the small random perturbation of the array shape may deteriorate the retrofocusing field but will not induce focal shift. If there is constant difference between expectation values of the actual and fictitious sound speed profiles or array shapes, the mirages might appear under the mismatches.

## II. IMAGING THROUGH THE COHERENT SUMMATION OF VIRTUAL TIME REVERSAL FIELDS OVER FREQUENCY

Due to the mismatches of sound speed profile and array shape, the virtual time reversal field, which is sensitive to the inaccuracies of model parameters, would be degraded seriously. The spurious spots in virtual time reversal field prevent us to identify true source position. The virtual time reversal field is frequency dependent, and the speckle noise appears randomly in the searching domain at different frequencies. Nevertheless, the focal position near the original source is statistical stable in despite of the degradation of virtual time reversal field.

### A. Imaging algorithm

A straightforward idea to image active sources in shallow water waveguide is by summing up or taking average value of the virtual time reversal fields to smooth the random speckle noise and highlight the focal spots. We construct the imaging estimator with the coherent summation of virtual time reversal fields over frequency band of the probe signal

$$\mathcal{I}(\mathbf{r}; \Omega_d) = \int_{\mathcal{B}} d\omega \int_{\mathcal{B}} d\omega' \mathbf{1}_{\{|\omega - \omega'| \leq \Omega_d\}}(\omega) \Gamma(\mathbf{r}, \omega) \Gamma^*(\mathbf{r}, \omega'), \quad (35)$$

where  $\mathcal{B}$  is the frequency band of the probe source,  $\Omega_d$  is frequency segmentation parameter, and  $\Gamma$  is the virtual time reversal field given in Eq. (2). The indicator function is defined as

$$\mathbf{1}_A(\omega) = \begin{cases} 1 & \text{if } \omega \in A, \\ 0 & \text{if } \omega \notin A, \end{cases} \quad (36)$$

which acts as a rectangular frequency decoherence window.

Equation (35) is in fact a reduced form of coherent interferometry<sup>17,18</sup>, in which the frequency decoherence is taken into consideration while the array length decoherence is ignored. That is because after long range propagation, the acoustic field in waveguide becomes highly correlated in the vertical direction<sup>15,23,24</sup>. The frequency segmentation parameter could be adjusted to smooth the image, and over the optimal one, the virtual time reversal fields

become statistically uncorrelated. Ignoring array length decoherence enable us to calculate virtual time reversal fields of each frequency components separately, thus to develop algorithm parallelization.

In case of infinitely small frequency segmentation parameter  $\Omega_d = 0$ , and replace the indicator function with the Dirac function, we get the conventional matched field processing estimator<sup>4,16</sup>

$$\mathcal{I}(\mathbf{r}; 0) = \int_{\mathcal{B}} d\omega |\Gamma(\mathbf{r}, \omega)|^2 = \mathcal{I}^{\text{MF}}(\mathbf{r}). \quad (37)$$

The matched field processing estimator is a incoherent summation of virtual time reversal fields.

If we open the frequency decoherence window to the full band or even infinitely by setting the frequency segmentation parameter as  $\Omega_d = \infty$ , then we get the amplitude square of Kirchhoff migration estimator<sup>16,25</sup>

$$\mathcal{I}(\mathbf{r}; \infty) = \left| \int_{\mathcal{B}} d\omega \Gamma(\mathbf{r}, \omega) \right|^2 = |\mathcal{I}^{\text{KM}}(\mathbf{r})|^2. \quad (38)$$

The Kirchhoff migration estimator, which is mostly used in exploration geophysics, is a direct summation of virtual time reversal fields.

We give the image function in a normalized square root form

$$\mathcal{J}(\mathbf{r}; \Omega_d) = \frac{\sqrt{|\mathcal{I}(\mathbf{r}; \Omega_d)|}}{\sup_{\mathbf{r} \in \mathcal{D}} \sqrt{|\mathcal{I}(\mathbf{r}; \Omega_d)|}}, \quad (39)$$

and plot in the logarithmic coordinate system

$$\mathcal{TL}(\mathbf{r}; \Omega_d) = -20 \log_{10} \mathcal{J}(\mathbf{r}; \Omega_d). \quad (40)$$

## B. Optimal frequency segmentation parameter selection

The different selection of the frequency segmentation parameter plays an important role in imaging process, and it is rather practical. We determine the optimal one  $\Omega_d^*$  by using the criterion based on the image quality, that is by minimizing the objective function<sup>16</sup>

$$\Omega_d^* = \arg \min_{\Omega_d} \|\mathcal{J}(\mathbf{r}; \Omega_d)\|_{\text{BV}}, \quad (41)$$

where the bounded variation norm of the image function is defined as<sup>26</sup>

$$\begin{aligned}\|\mathcal{J}(\mathbf{r}; \Omega_d)\|_{\text{BV}} &= \|\mathcal{J}(\mathbf{r}; \Omega_d)\|_{L^1(\mathcal{D})} + \alpha \|\nabla \mathcal{J}(\mathbf{r}; \Omega_d)\|_{L^1(\mathcal{D})} \\ &= \int_{\mathcal{D}} d\mathbf{r} (|\mathcal{J}(\mathbf{r}; \Omega_d)| + \alpha |\nabla \mathcal{J}(\mathbf{r}; \Omega_d)|). \end{aligned} \quad (42)$$

The first term on the right side of Eq. (42) corresponds to the stability of the image, while the second term denotes the image sharpness. The adjustive parameter  $\alpha$  should be properly calibrated, and a good balance value is  $\alpha = 1$ .

### C. Imaging resolution estimation

Due to the absorption and reverberation in ocean waveguide, the higher-order normal modes will be eliminated in the two-way propagation in virtual time reversal process. The vertical length of the focal spot is mainly determined by the number of remainder modes, while the horizontal length is determined by the difference of the biggest and smallest horizontal wavenumbers, which is the smallest interference pattern in waveguide<sup>6</sup>. As we construct the imaging estimator by summing up the virtual time reversal fields over the full frequency band of the probe signal, the imaging resolution approximates to the focal spot size at the central frequency of the probe signal. The depth and range resolutions at 3 dB down points could be roughly estimated as<sup>8,27</sup>

$$L_z \sim \frac{D}{M(\omega_0)}, \quad (43)$$

$$L_r \sim \frac{2\pi}{\kappa_{01}(\omega_0) - \kappa_{0M}(\omega_0)}, \quad (44)$$

respectively. Here  $\omega_o$  is the central frequency of the probe signal,  $M$  is the mode number, and  $\kappa_{01}$  and  $\kappa_{0M}$  are the real parts of the biggest and smallest unperturbed horizontal wavenumbers, respectively.

### D. Numerical experiments

In this part, we present numerical simulation results of time reversal imaging in stratified waveguide. The experimental setups of the waveguide and the array are exactly as same as

that are given in the previous section. To image, two active sources are deployed, one is located at the depth of 40 m and the range of 0 km, and another is at the depth of 70 m and the range of 1 km. The probe signal waveforms are both selected as

$$f(\omega) = i\omega e^{-\frac{(\omega-\omega_0)^2}{2\sigma^2}} \mathbf{1}_{[\omega_0-B/2, \omega_0+B/2]}, \quad (45)$$

where  $\sigma = 2.87$ , the central frequency is at 375 Hz, and the frequency band width is  $B = 150$  Hz. The truncated frequency band  $\mathcal{B} = [300, 450]$  Hz is sampled with 0.5 Hz frequency interval. Fig. 5 depicts the spectrum of the probe source. Our computation of sound wave propagation is performed in the frequency domain through normal mode program Kraken<sup>28</sup>.

The simulations are performed in four different circumstances, i.e., unperturbed sound speed profile and array shape, the mismatch of sound speed profile, the mismatch of array shape, and the mismatches of sound speed profile and array shape. In Fig. 6, we find in each circumstance, broadening in frequency decoherence window decreases the objective function progressively, that the Kirchhoff migration estimator achieves best image quality. We compare the images with minimum, 5 Hz, and full band frequency segmentation parameters.

### ***1. Imaging under unperturbed sound speed profile and array shape***

We first give the time reversal imaging results in unperturbed waveguide with an unperturbed array. In deterministic case, there is no perturbation, that the images are not deteriorated. Two probe sources are deployed, one is located at the depth of 40 m and the range of 0 km, and another is put at the depth of 70 m and the range of 1 km. The vertical array is at the range of 8 km.

Figure 7 (a) is an image with minimum frequency segmentation parameter. The conventional matched field processing estimator is the incoherent summation of virtual time reversal fields, in which only the amplitude information is used while the phase information is discarded. We can see in deterministic circumstance, the conventional matched field processing estimator can clearly identify two active probe sources, and the background is smoothed compared with virtual time reversal field at single frequency. When the frequency



segmentation parameter is adjusted to 5 Hz, the background level is decreased that the image quality is improved, as presented in Fig. 7 (b). Fig. 7 (c) shows an image of Kirchhoff migration estimator, in which we can see when the frequency segmentation parameter is adjusted to the full band, the focal spots appear extremely clear and bright, while the background becomes more smooth and dark. Enlarging the frequency decoherence window improves the image quality.

To see the resolutions of time reversal imaging, we only turn on the active source at the depth of 40 m and the range of 0 km, but turn off another one. In the imaging process, we sum the virtual time reversal fields over the frequency band of the probe source, thus the imaging resolutions approximate the focal spot sizes of the virtual time reversal field at the central frequency of the probe source. In Figs. 8 (a) - (b) we see the horizontal and vertical resolutions of the images of different frequency parameters approximate the horizontal and vertical focal lengths of the virtual time reversal field at 375 Hz, respectively. Fig. 9 presents the complex horizontal wavenumbers of the unperturbed waveguide, in which we see the difference between the largest and smallest horizontal wavenumbers is about  $0.378 \text{ m}^{-1}$ , which determine the horizontal focal length, and the mode number is 33, which determine the vertical focal length. Thus the horizontal and vertical imaging resolutions are about 16.6 m and 3.0 m measured at 3 dB down points, respectively.

## ***2. Imaging under the mismatch of sound speed profile***

The sound speed profile mismatch introduces horizontal wavenumber and normal mode shape function perturbations. The time reversal invariant is ruined that the virtual time reversal field would be degraded and focal spots might not correspond to the original sources. The summation of virtual time reversal fields over frequency band could highlight the focal spots and smooth background, that help us to locate sources in perturbed waveguide.

Figure 10 (a) is an image of the conventional matched field processing estimator under the mismatch of sound speed profiles, where the focal spots appear extremely weak that could

not be easily identified. This is because the incoherent summation could not clearly smooth the heterogeneous background of perturbed virtual time reversal fields. In Figs. 10 (b) - (c), we plot the imaging results with 5 Hz and full band frequency decoherence windows, respectively. Increasing frequency decoherence parameter brings a distinct improvement of image quality. The sound speed profile mismatch deteriorates the images, that the focal spots are enlarged and side lobes raise.

### ***3. Imaging under the mismatch of array shape***

This part presents the imaging performance under of array shape mismatch. The perturbation of array sampling position would introduce the signal perturbation recorded by the receivers.

Figure 11 (a) is an image of conventional matched field processing estimator, Fig. 11 (b) is an image with 5 Hz frequency segmentation parameter, and Fig. 11 (c) is an image of Kirchhoff migration estimator. We can see that the random array shape perturbation decrease the brightness of focal spots, but the imaging resolution is not deteriorated.

### ***4. Imaging under the mismatches of sound speed profile and array shape***

When there exist the sound speed profile and array shape mismatches, the image with matched field processing estimator is totally rubbed away that the original source positions could not be recovered, as shown in Fig. 12 (a). Imaging with 5 Hz frequency segmentation parameter in Fig. 12 (b), there are two big vertical bars which correspond to two active probe sources, but it is almost impossible for us to extract the depth information. Fig. 12 (c) shows the imaging result with Kirchhoff migration estimator. We see that when the frequency segmentation parameter is adjusted to the maximum, the source range information can be retrieved but there are side lobes in the vertical direction which prevent use to identify the source depths exactly.

We have performed time reversal imaging under different realizations of sound speed

profile and array shape mismatches, and the results indicate the method is robust in locating active sources.

### III. IMAGE QUALITY IMPROVEMENT BY FILTERING PERTURBED NORMAL MODES

The sound speed profile mismatch causes the mode shape function and corresponding horizontal wavenumber perturbations, thus the virtual time reversal fields are degraded and imaging results will be deteriorated. In Fig. 2 we have seen that the lower modes are perturbed enormously while the higher modes appear almost invariable. We propose to improve the image quality by filtering out the perturbed modes.

#### A. Mode selection criterion

We first define the mode projection coefficient matrix  $(c_{m'm})$ , whose element

$$c_{m'm} = (\varphi_{m'}(z), \varphi_{0m}(z)) \quad (46)$$

is the projection of  $m'$ th actual mode shape function  $\varphi_{m'}(z)$  onto the  $m$ th basis of the complete orthonormal set  $\{\varphi_{0m}\}$ .

The energy distribution ratio coefficient is given by

$$\beta_m = \frac{\sum_{m' \neq m} |c_{m'm}|^2}{|c_{mm}|^2}, \quad (47)$$

in which the denominator denotes the preserved energy of the actual mode at corresponding fictitious mode basis, while the numerator means the energy distributed onto to the rest bases.

The mode selection set is defined as

$$\mathcal{M} = \{m : \beta_m \leq \beta\}, \quad (48)$$

in which the threshold value could be defined as  $\beta = 1$ , that if the preserved energy is less than that is distributed, we get ride of this mode, otherwise kept it.

In following parts, we introduce two methods to achieve mode filtering to improve image quality: one is through filtering the array received acoustic pressure, and another is through truncating virtual time reversal field.

## B. Mode selection through filtering array signal

In the imaging process, the vertical array receive acoustic pressure signal, which could be expanded by the complete orthonormal set

$$p(z) = \sum_m a_m \varphi_{0m}(z), \quad (49)$$

where the expansion coefficient  $a_m$  is

$$a_m = (p(z), \varphi_{0m}(z)). \quad (50)$$

If we keep the modes in the set  $\mathcal{M}$  and filter out others, the filtered acoustic pressure becomes

$$p'(z) = \sum_{m \in \mathcal{M}} a_m \varphi_{0m}(z). \quad (51)$$

The processed acoustic pressure signal is then time reversed and sent back into a fictitious waveguide.

In this method, we need a full-spanned and dense array to extract expansion coefficients and avoid mode leakage.

## C. Mode selection through truncating virtual time reversal fields

In the imaging processing, the virtual time reversal fields are summed over the frequency band, which could be expressed as a summation of each mode components

$$\Gamma(\mathbf{r}) = \sum_m \Gamma_m(\mathbf{r}). \quad (52)$$

To filter out perturbed modes, we only need to keep the selected modes in the set

$$\Gamma'(\mathbf{r}) = \sum_{m \in \mathcal{M}} \Gamma_m(\mathbf{r}). \quad (53)$$

This method can be easily realized in the procedure of calculating virtual time reversal fields, and it also relieves computational load. We only need to add selected modes and discard others. The processed virtual time reversal fields can then be used to construct imaging estimators.

Both of these two methods get rid of the mode components projected in the subspace  $\{\varphi_{0m}\}_{\mathbb{N}\setminus\mathcal{M}}$ , and they in fact achieve the same effect.

#### D. Numerical results

In this part, the numerical simulation of time reversal imaging by filtering out perturbed modes are presented, and the results are compared with original images. We filter modes through truncating virtual time reversal fields, as this method is fast and easy to realize.

The sound speed mismatch will cause the mode perturbation, thus the actual and fictitious mode shape functions become quasi-orthonormal. In the top-left corner of the mode projection coefficient matrix shown in Fig. 13, the orthogonality of lower order modes is ruined, but in the lower-right corner, which indicates higher orders, the mode shape functions are nearly orthonormal. From the graphical representation of mode projection coefficient matrix, we also find the lower order modes are mainly perturbed. Fig. 14 shows the ratio coefficient of energy distribution, in which we see more proportion of energy is distributed in lower orders. In our mode filtering process, the first 6 order modes are excluded while the rest are kept.

Figures 15 (a) - (b) present the horizontal slices of the images with matched field processing estimator under sound speed profile mismatch, which are normalized at the ranges of sources. We can find that after the mode filtering process, the background level is decreased, which means the focal spots are highlighted, and the horizontal focal spot length has been narrowed, which mean the focal spots become sharper. Figs. 15 (c) - (d) show the vertical slices, and they are normalized at depths of sources. We see filtering out perturbed modes will suppress the side lobes, that the depths of original sources can be determined with out

ambiguous. Fig. 16 and Fig. 17 give the original and filtered imaging results with 5 Hz and maximum frequency decoherence parameter, respectively. The image quality improvements are also presented similarly.

In practical imaging operation, the actual sound speed profile of physical waveguide is not always available, that means we can not determine the mode selection set. A simple solution is to use try-and-test strategy that we gradually cut off lower order modes to see the image quality improvement.

#### IV. SUMMARY

The presence of the mismatches between actual and fictitious sound speed profiles and array shapes deteriorates the virtual time reversal fields. The process of the coherent summation of virtual time reversal field over the frequency band of probe signal will highlight focal spots, as well as smooth the heterogeneous background, which help us to identify the original source positions clearly. We find that maximum frequency decoherence window will achieve best imaging result in range-independent waveguide. Filtering out perturbed modes with the selection criterion based on the energy distribution ratio of the mode shape functions improves the image quality. The virtual time reversal fields of each frequency components can be calculated separately to accelerate the imaging process.

#### Acknowledgments

The author would like to thank Dr. Y. Wu for discussions and financial support from the start-up fund package at KAUST.

#### References

- <sup>1</sup> M. Hayes and P. Gough, "Broad-band synthetic aperture sonar", IEEE J. of Oceanic Eng. **17**, 80–94 (1992).

- <sup>2</sup> X. Lurton, *An introduction to underwater acoustics: principles and applications* (Springer-Praxis) (2002).
- <sup>3</sup> A. Tolstoy, *Matched field processing for underwater acoustics*, volume 52 (World Scientific Singapore) (1993).
- <sup>4</sup> A. Baggeroer, W. Kuperman, and P. Mikhalevsky, “An overview of matched field methods in ocean acoustics”, *IEEE J. of Oceanic Eng.* **18**, 401–424 (1993).
- <sup>5</sup> G. L. D’Spain, J. J. Murray, W. S. Hodgkiss, N. O. Booth, and P. W. Schey, “Mirages in shallow water matched field processing”, *J. Acoust. Soc. Am.* **105**, 3245–3265 (1999).
- <sup>6</sup> W. Kuperman, W. Hodgkiss, H. Song, T. Akal, C. Ferla, and D. Jackson, “Phase conjugation in the ocean: Experimental demonstration of an acoustic time-reversal mirror”, *J. Acoust. Soc. Am.* **103**, 25–40 (1998).
- <sup>7</sup> W. S. Hodgkiss, H. C. Song, W. A. Kuperman, T. Akal, C. Ferla, and D. R. Jackson, “A long-range and variable focus phase-conjugation experiment in shallow water”, *J. Acoust. Soc. Am.* **105**, 1597–1604 (1999).
- <sup>8</sup> S. Kim, W. A. Kuperman, W. S. Hodgkiss, H. C. Song, G. F. Edelmann, and T. Akal, “Robust time reversal focusing in the ocean”, *J. Acoust. Soc. Am.* **114**, 145–157 (2003).
- <sup>9</sup> P. Roux and M. Fink, “Time reversal in a waveguide: Study of the temporal and spatial focusing”, *J. Acoust. Soc. Am.* **107**, 2418–2429 (2000).
- <sup>10</sup> M. Fink and C. Prada, “Acoustic time-reversal mirrors”, *Inverse Problems* **17**, R1 (2001).
- <sup>11</sup> H. C. Song, W. A. Kuperman, and W. S. Hodgkiss, “A time-reversal mirror with variable range focusing”, *J. Acoust. Soc. Am.* **103**, 3234–3240 (1998).
- <sup>12</sup> P. Blomgren, G. Papanicolaou, and H. Zhao, “Super-resolution in time-reversal acoustics”, *J. Acoust. Soc. Am.* **111**, 230–248 (2002).
- <sup>13</sup> G. Papanicolaou, L. Ryzhik, and K. Sølna, “Statistical stability in time reversal”, *SIAM Journal on Applied Mathematics* 1133–1155 (2004).
- <sup>14</sup> L. Borcea, G. Papanicolaou, C. Tsogka, and J. Berryman, “Imaging and time reversal in random media”, *Inverse Problems* **18**, 1247 (2002).
- <sup>15</sup> L. Borcea, L. Issa, and C. Tsogka, “Source localization in random acoustic waveguides”,

- Multiscale Modeling & Simulation **8**, 1981–2022 (2010).
- <sup>16</sup> L. Borcea, G. Papanicolaou, and C. Tsogka, “Adaptive interferometric imaging in clutter and optimal illumination”, *Inverse Problems* **22**, 1405 (2006).
  - <sup>17</sup> L. Borcea, G. Papanicolaou, and C. Tsogka, “Interferometric array imaging in clutter”, *Inverse Problems* **21**, 1419 (2005).
  - <sup>18</sup> L. Borcea, G. Papanicolaou, and C. Tsogka, “Theory and applications of time reversal and interferometric imaging”, *Inverse Problems* **19**, S139 (2003).
  - <sup>19</sup> L. Borcea, G. Papanicolaou, and C. Tsogka, “A resolution study for imaging and time reversal in random media”, *Contemporary Mathematics* **333**, 63–78 (2003).
  - <sup>20</sup> C. T. Tindle, L. M. O’Driscoll, and C. J. Higham, “Coupled mode perturbation theory of range dependence”, *J. Acoust. Soc. Am.* **108**, 76–83 (2000).
  - <sup>21</sup> G. Frisk, *Ocean and seabed acoustics: a theory of wave propagation* (Prentice Hall) (1994).
  - <sup>22</sup> F. B. Jensen, W. A. Kuperman, M. B. Portor, and H. Schmidt, *Computational ocean acoustics*, AIP series in modern acoustics and signal processing (American Institute of Physics) (1993).
  - <sup>23</sup> L. Dozier and F. Tappert, “Statistics of normal mode amplitudes in a random ocean”, *J. Acoust. Soc. Am.* **61**, 353–365 (1977).
  - <sup>24</sup> J. Fouque, J. Garnier, G. Papanicolaou, and K. Solna, *Wave propagation and time reversal in randomly layered media*, volume 56 (Springer Verlag) (2007).
  - <sup>25</sup> N. Bleistein, J. Cohen, and J. Stockwell, *Mathematics of multidimensional seismic imaging, migration, and inversion*, volume 13 (Springer Verlag) (2001).
  - <sup>26</sup> E. Giusti, *Minimal surfaces and functions of bounded variation*, volume 80 (Birkhauser) (1984).
  - <sup>27</sup> S. Kim, G. F. Edelmann, W. A. Kuperman, W. S. Hodgkiss, H. C. Song, and T. Akal, “Spatial resolution of time-reversal arrays in shallow water”, *J. Acoust. Soc. Am.* **110**, 820–829 (2001).
  - <sup>28</sup> M. Porter, “The kraken normal mode program”, Technical Report, DTIC Document (1992).



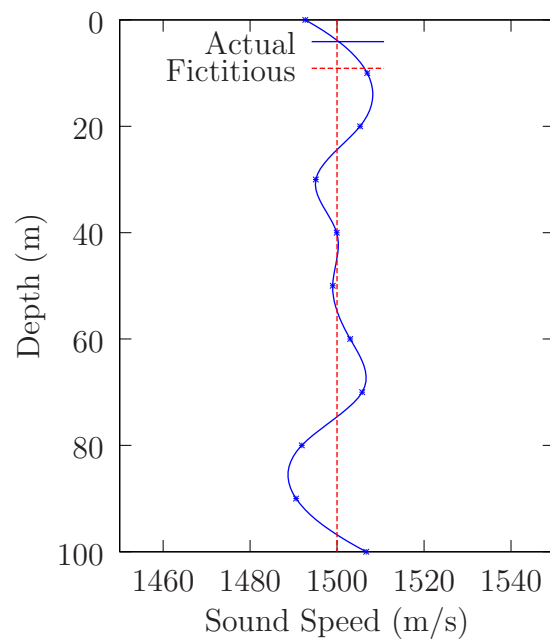


FIG. 1.

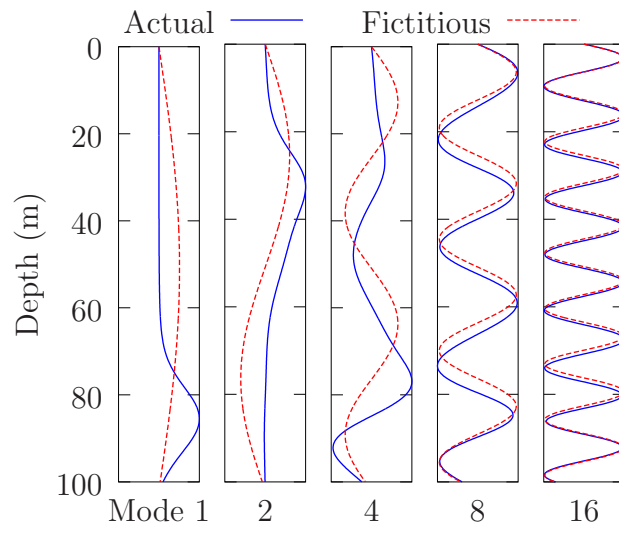
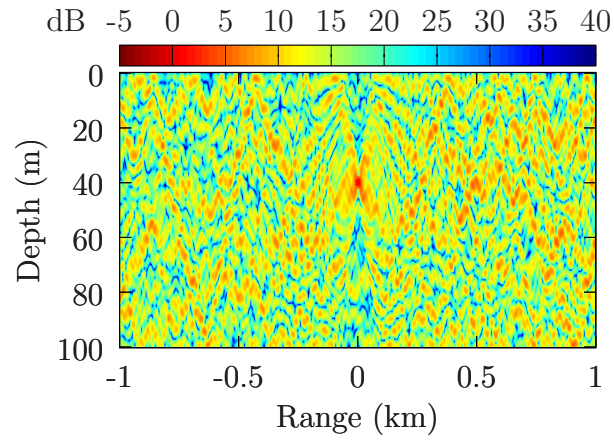
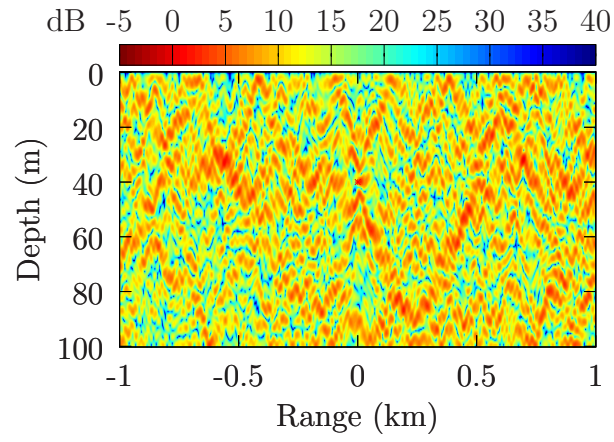


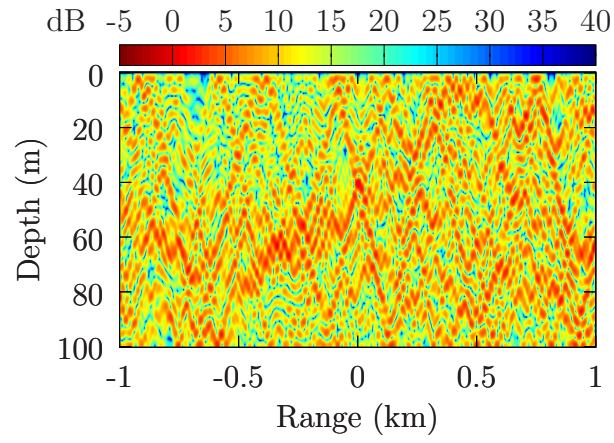
FIG. 2.



(a)



(b)



(c)

FIG. 3.

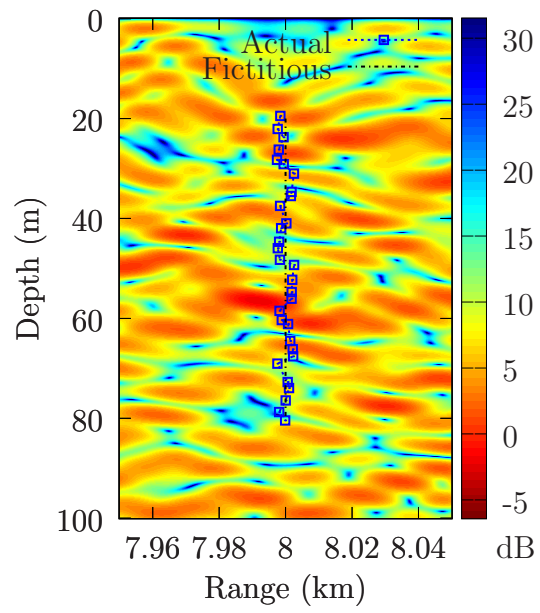


FIG. 4.

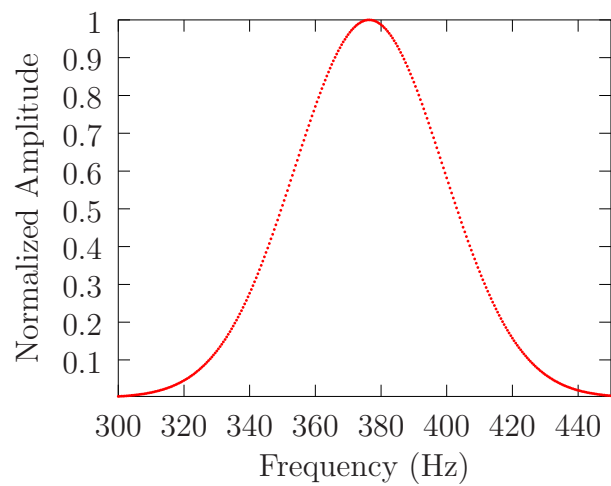


FIG. 5.

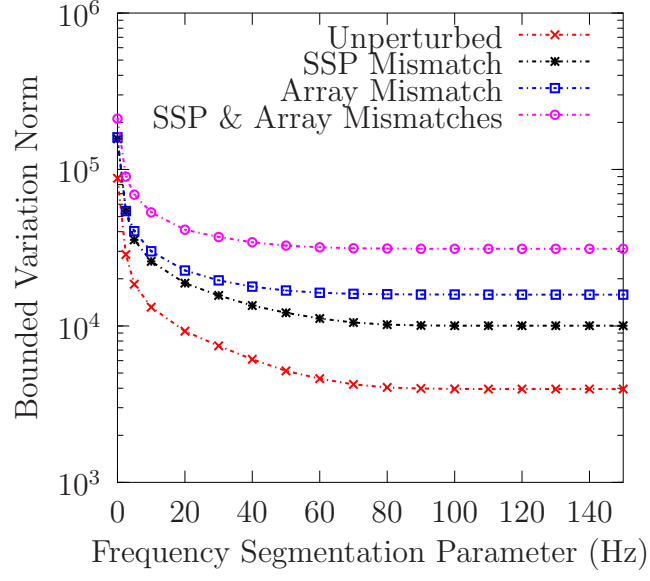
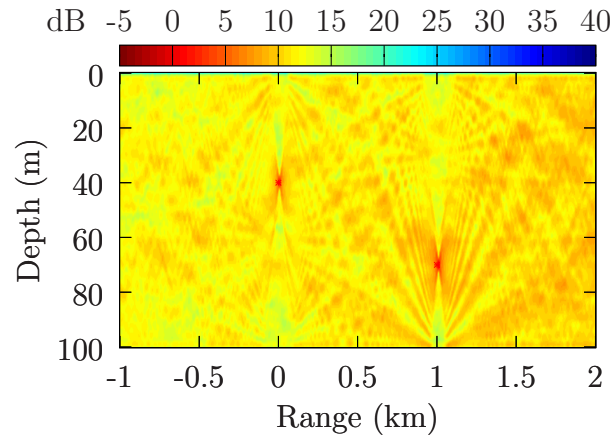
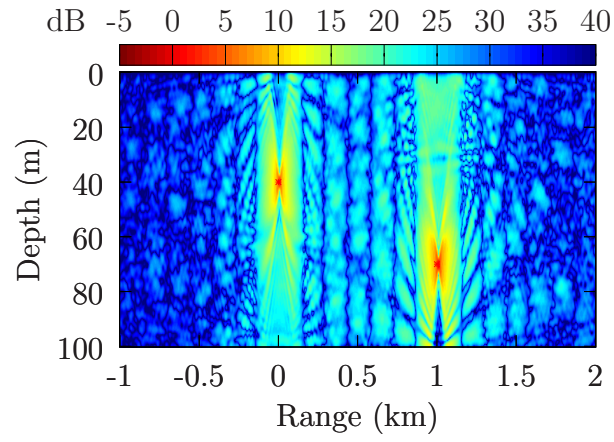


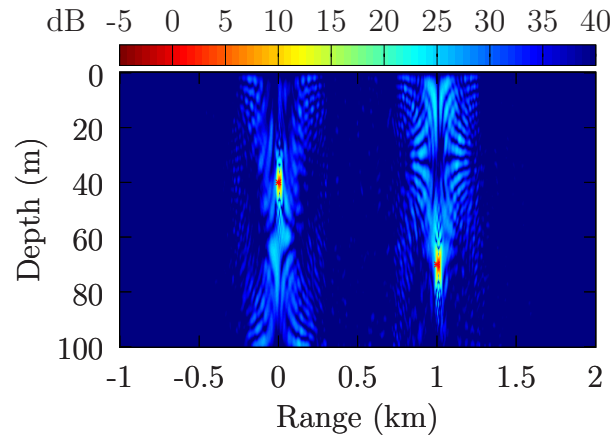
FIG. 6.



(a)

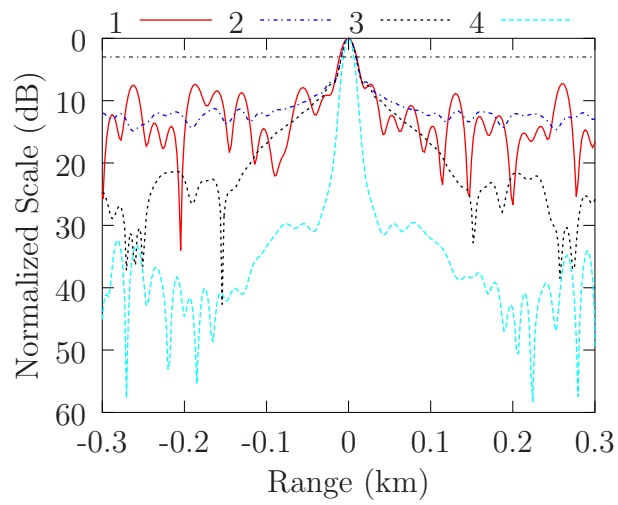


(b)

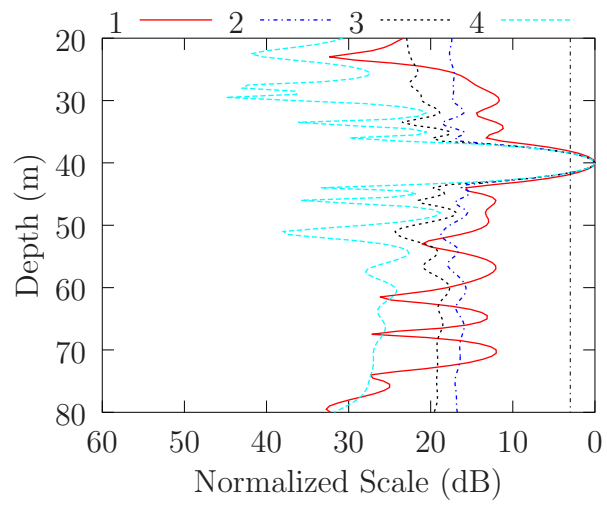


(c)

FIG. 7.



(a)



(b)

FIG. 8.



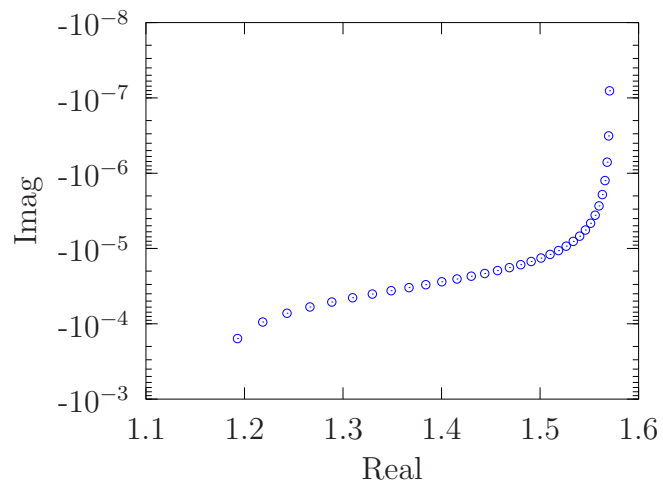
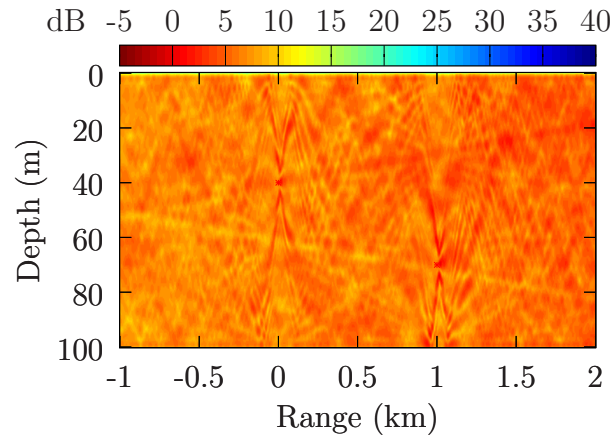
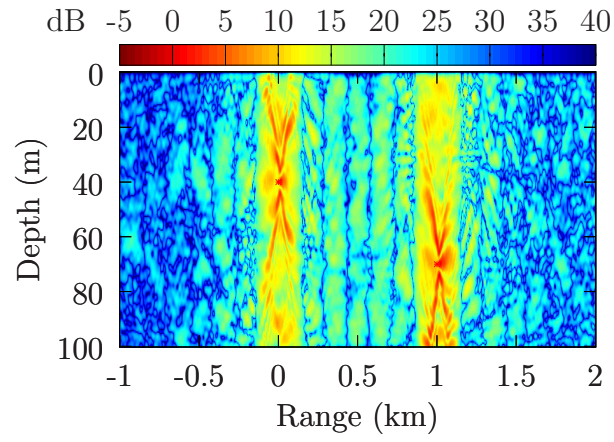


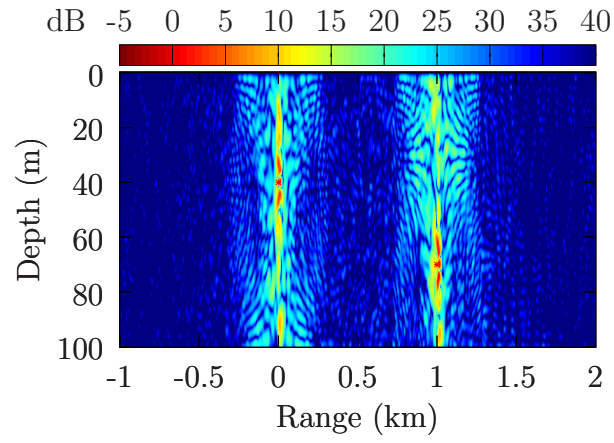
FIG. 9.



(a)

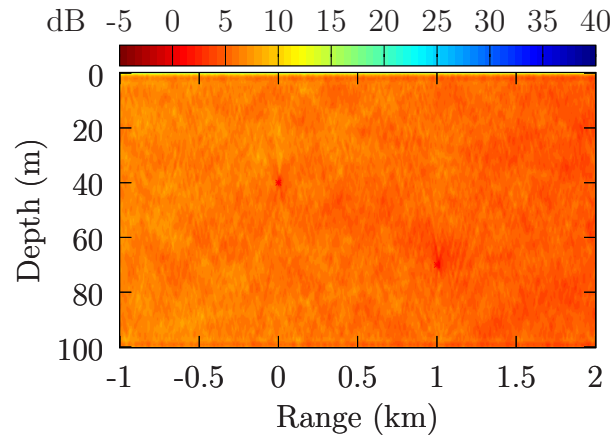


(b)

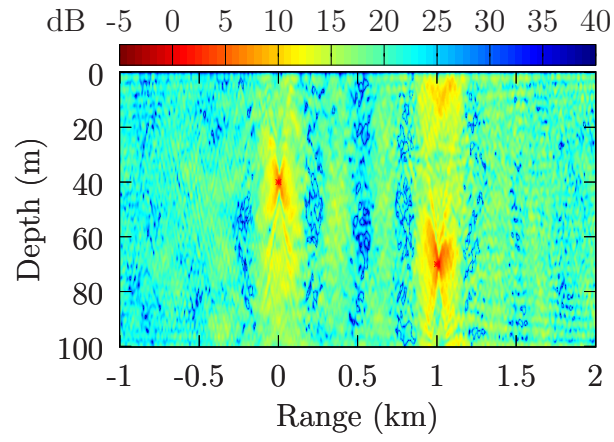


(c)

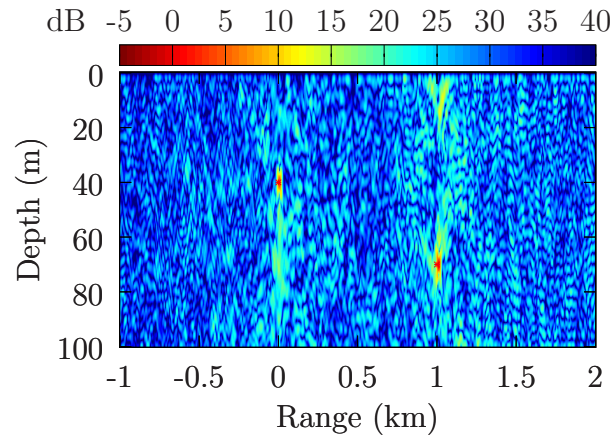
FIG. 10.



(a)

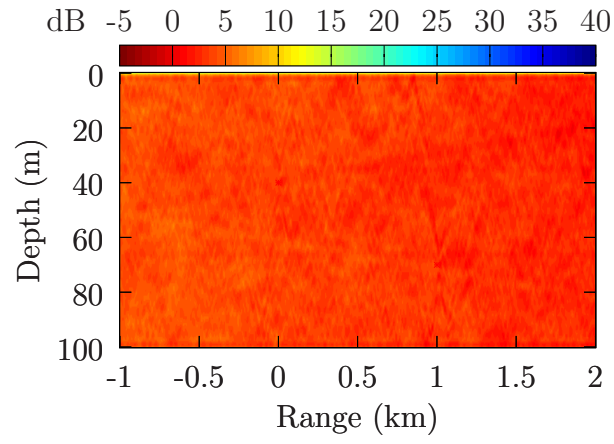


(b)

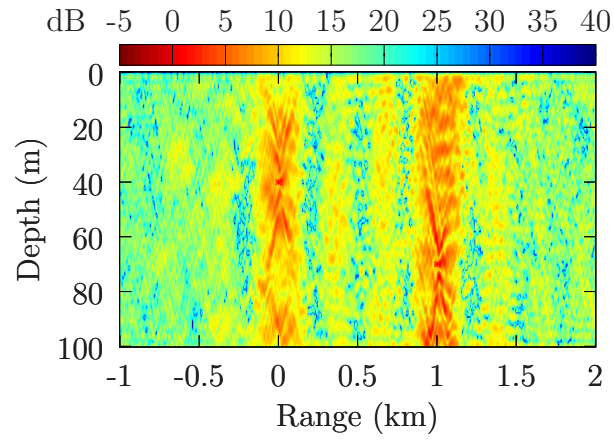


(c)

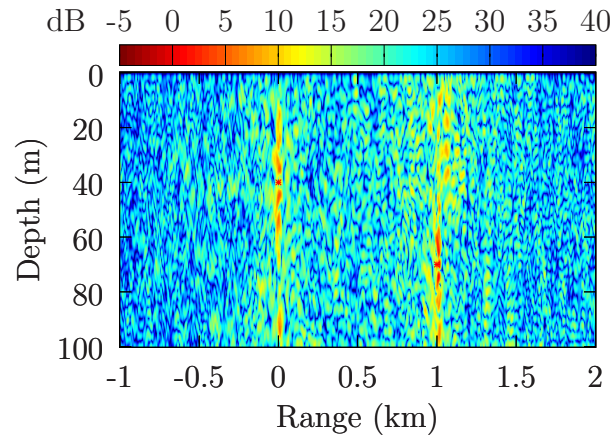
FIG. 11.



(a)



(b)



(c)

FIG. 12.

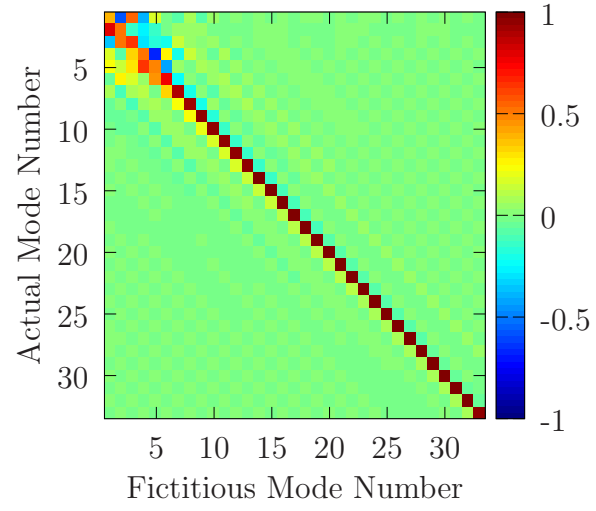


FIG. 13.

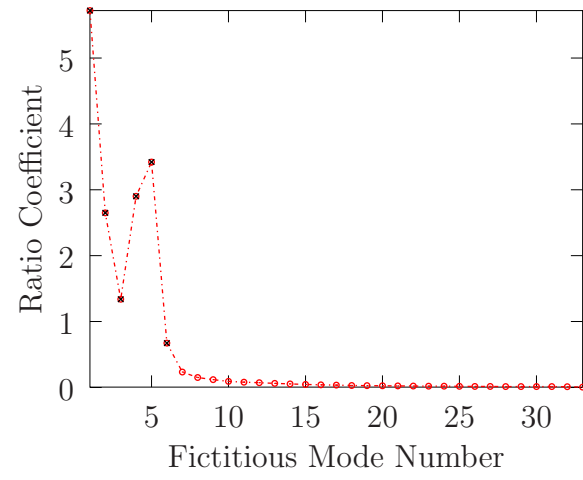
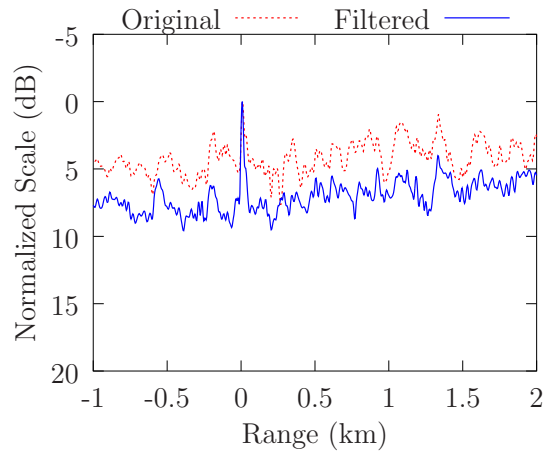
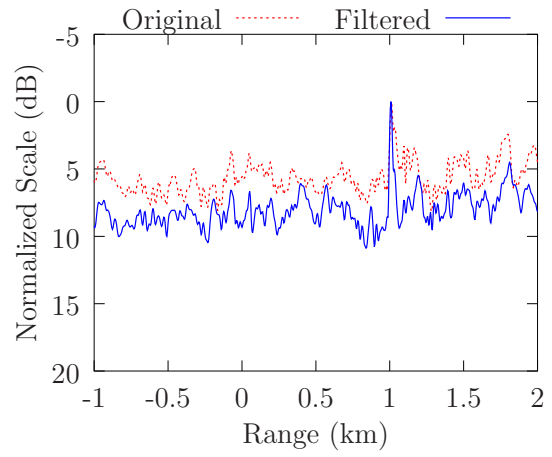


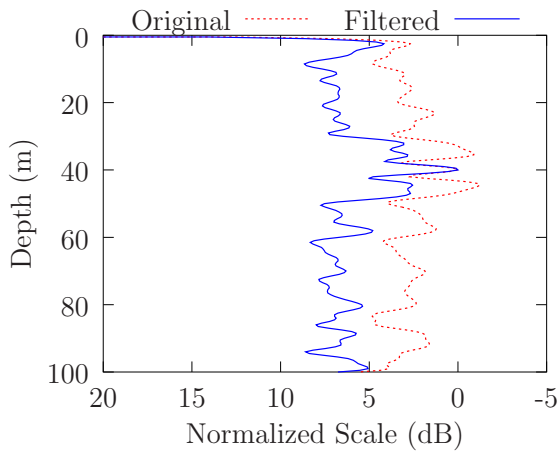
FIG. 14.



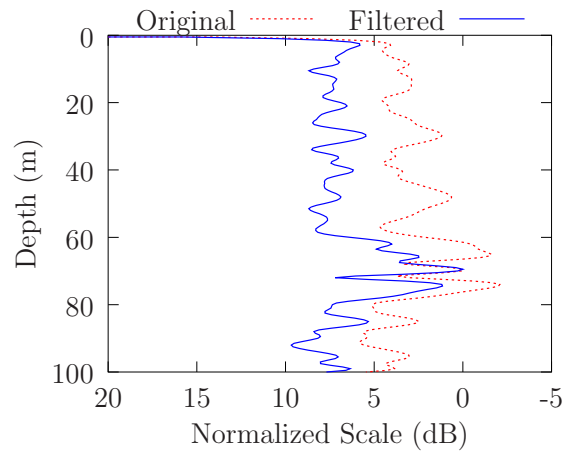
(a)



(b)



(c)



(d)

FIG. 15.

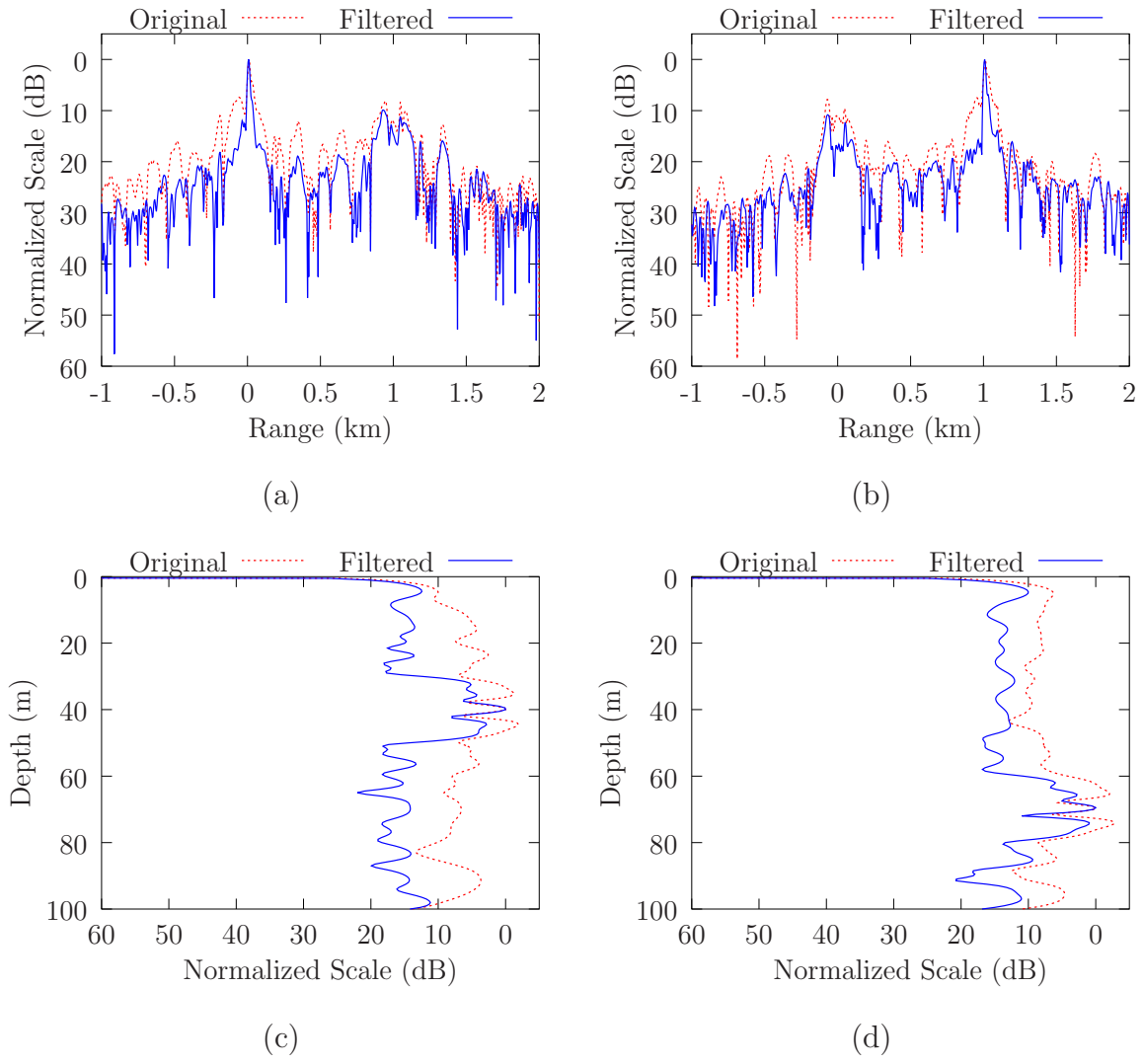


FIG. 16.



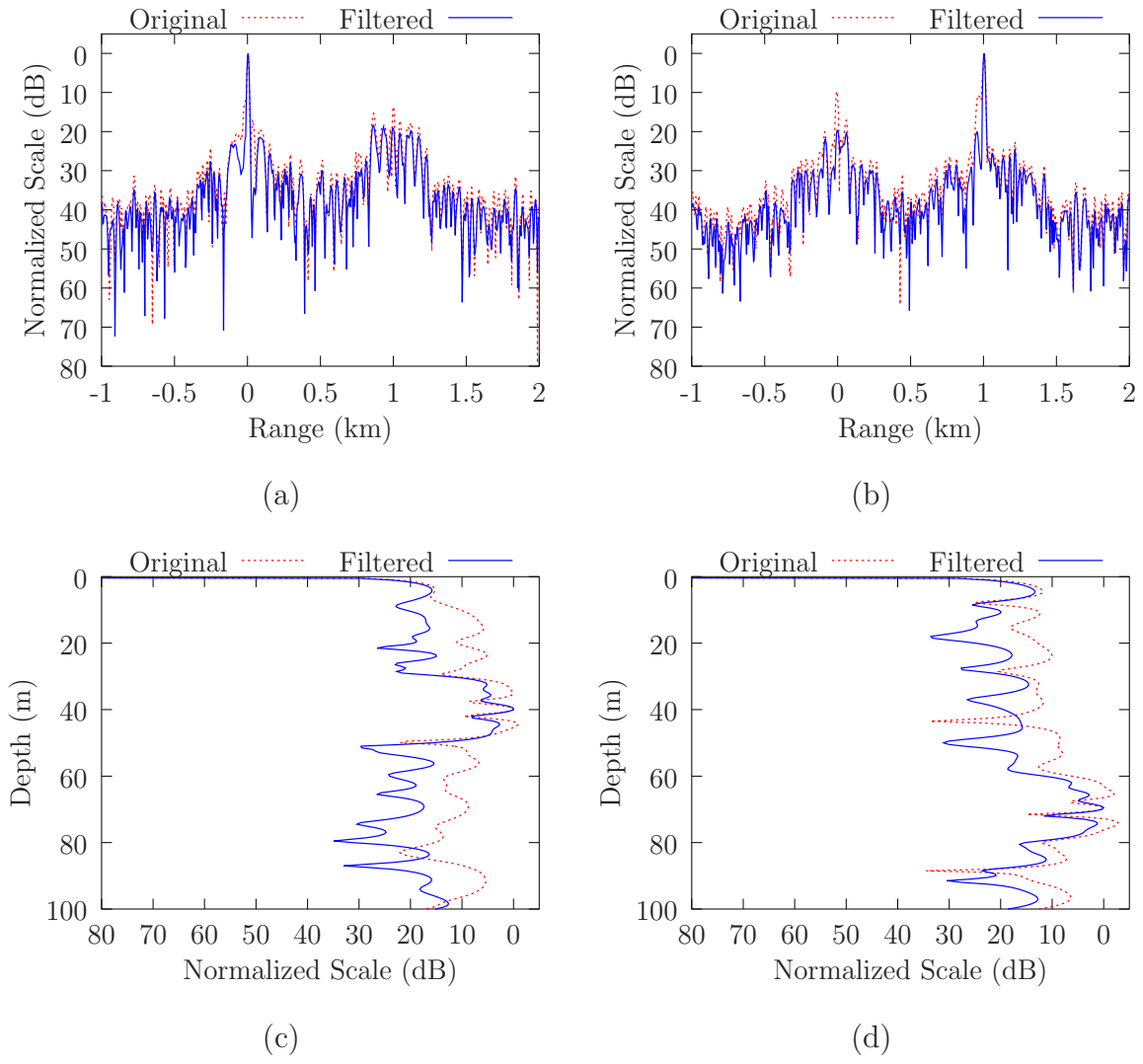


FIG. 17.

## List of Figures

FIG. 1	Sound speed profile mismatch. . . . .	25
FIG. 2	Mode shape function perturbation. . . . .	26
FIG. 3	Virtual time reversal fields at 375 Hz. A single probe source is located at the depth of 40 m and the range of 0 km. The vertical array is at the range of 8 km. (a) A snapshot of the retrofocusing field in unperturbed waveguide with an unperturbed array. (b) A snapshot of the retrofocusing field under sound speed profile mismatch. (c) A snapshot of the retrofocusing field under array shape mismatch. . . . .	27
FIG. 4	Array shape mismatch. . . . .	28
FIG. 5	Spectrum of the probe signal. . . . .	29
FIG. 6	Objective functions in different circumstances. . . . .	30
FIG. 7	Imaging results in unperturbed waveguide with unperturbed array. There are two probe sources, one is located at the depth of 40 m and the range of 0 km, and another is at the depth of 70 m and the range of 1 km. The vertical array is at the range of 8 km. (a) Image of minimum frequency segmentation parameter. (b) Image of 5 Hz frequency segmentation parameter. (c) Image of maximum frequency segmentation parameter. . . . .	31
FIG. 8	Imaging resolutions. (a) Horizontal slices at the depth of 40 m. (b) Vertical slices at the range of 0 km. In the legend, 1 denotes the slice of virtual time reversal field at 375 Hz, 2 denotes the slice of the image of minimum frequency segmentation parameter, 3 denotes the slice of the image of 5 Hz frequency segmentation parameter, and 4 denotes the slice of the image of maximum frequency segmentation parameter. . . . .	32
FIG. 9	Horizontal wavenumbers of the unperturbed waveguide at 375 Hz. . . . .	33

FIG. 10 Imaging results under the mismatch of sound speed profile. (a) Image of minimum frequency segmentation parameter. (b) Image of 5 Hz frequency segmentation parameter. (c) Image of maximum frequency segmentation parameter. . . . .	34
FIG. 11 Imaging results under the mismatch of array shape. (a) Image of minimum frequency segmentation parameter. (b) Image of 5 Hz frequency segmentation parameter. (c) Image of maximum frequency segmentation parameter. . . .	35
FIG. 12 Imaging results under the mismatches of sound speed profile and array shape. (a) Image of minimum frequency segmentation parameter. (b) Image of 5 Hz frequency segmentation parameter. (c) Image of maximum frequency segmentation parameter. . . . .	36
FIG. 13 Orthonormal relationship between the actual and fictitious mode shape functions. . . . .	37
FIG. 14 Energy distribution ratio. . . . .	38
FIG. 15 Slices of the images of minimum frequency segmentation parameter after mode filtering, which are normalized by the value at the source positions. (a) Horizontal slices at the depth of 40 m. (b) Horizontal slices at the depth of 70 m. (c) Vertical slices at the range of 0 km. (d) Vertical slices at the range of 1 km. . . . .	39
FIG. 16 Slices of the images of 5 Hz frequency segmentation parameter after mode filtering, which are normalized by the value at the source positions. (a) Horizontal slices at the depth of 40 m. (b) Horizontal slices at the depth of 70 m. (c) Vertical slices at the range of 0 km. (d) Vertical slices at the range of 1 km. . . . .	40

FIG. 17 Slices of the images of maximum frequency segmentation parameter after mode filtering, which are normalized by the value at the source positions. (a) Horizontal slices at the depth of 40 m. (b) Horizontal slices at the depth of 70 m. (c) Vertical slices at the range of 0 km. (d) Vertical slices at the range of 1 km. . . . . 41